Supplementary Materials for

Integrated Compact Optical Vortex Beam Emitters

Xinlun Cai, Jianwei Wang, Michael J. Strain, Benjamin Johnson-Morris, Jiangbo Zhu, Marc Sorel, Jeremy L. O'Brien, Mark G. Thompson, Siyuan Yu*

*To whom correspondence should be addressed. E-mail: s.yu@bristol.ac.uk

This PDF file includes:

> Materials and Methods
> Supplementary Text
> Figs. S1 to S7
> Full Reference List

Other Supplementary Material for this manuscript includes the following:
(available at www.sciencemag.org/cgi/content/full/338/6105/363/DC1)

> Movies S1 to S4

Materials and Methods

Device Structure and Fabrication

The PIC is fabricated on silicon-on-insulator (SOI) substrate, with 220-nm thick silicon as the waveguide layer. Both the access waveguide and the ring waveguide are 500-nm wide and 220-nm thick. The period of the grating is about 600-nm, corresponding to one wavelength in the ring waveguide to form a 2nd-order grating for the vacuum wavelength of 1530-nm. The grating elements protrude from the ring waveguide by as much as 60-nm, and their width is 60-nm, about 1/10 of the grating period. The gap between the ring and the straight waveguide is 100-200 nm. To reduce the coupling loss between the fibre and waveguide facet as well as the Fabry-Perot resonance effects caused by optical reflection from the facets, a coupling structure which consists of inversely tapered waveguides are fabricated at both end of the access waveguide. The structures are defined using electron-beam lithography which defines the PIC pattern in a negative e-beam resist, followed by an inductively coupled plasma etching process to transfer the PIC pattern into the silicon layer. Following the etching, a 300-nm-thick silicon dioxide layer is deposited onto the wafer to encapsulate the silicon waveguides. The above SOI platform has been widely used for other silicon PICs.

Experimental Setup using circularly polarised Gaussian reference beams

An experimental setup based on an interferometer configuration, as shown in Fig.S1, was used to study the intensity patterns and phase structure of the radiation beam. The single mode fibre output of a high precision tunable laser was split into two branches using a fibre coupler.

In one branch the laser power was coupled into one port of the PIC straight waveguide using a tapered fibre lens tip, with suitable power levels controlled by a variable optical attenuator (VOA). A fibre-optic polarization controller was used to launch light into the quasi-TE mode in the waveguide. In order to monitor the polarization, a polarizer followed by an optical power meter is arranged at the output port of the waveguide. When the laser wavelength coincides with a resonance of the micro-ring, the radiation beam is emitted, and then collimated by an objective lens.

In the other branch, the laser beam coming out of a flat-end fibre is directed to a collimator to produce an expanded and collimated Gaussian reference beam. After going through a linear polarizer followed by a quarter-wave plate set at 45 or -45 degrees to the axis of polarizer, the Gaussian beam is then LHCP or RHCP. The two branches are combined at a beam splitter and projected onto an infrared camera.

When the reference beam was turned off, we were able to image the near field intensity patterns of the radiated beams as shown in Fig. S2B. Fig. S2A shows the radiation spectra for a device with R=3.9 μm and q=36, measured by replacing the infrared camera with an optical power meter. The doublets in the spectrum result from the mode splitting caused by cross-coupling between the otherwise degenerate clockwise and counter-clockwise WGMs (*27*). The strongest cross-coupling occurs at the

wavelength with $p=q$ or $l=0$ due to second order Bragg reflection, therefore associated with the largest split (*28*).

When the reference beam was turned on, the phase structure of the radiated beam can be revealed by interference fringes (Fig. S2C, Fig. S2E), which are similar to the results from larger device in the main article (Fig. 3).

Fig. S2D and Fig. S2F show the semi-analytically simulated results, which agree very well with the measured results. They are calculated by replacing grating elements with dipole oscillators located at the same point where the grating elements are. The dipoles are polarized azimuthally and the phase difference between the adjacent dipoles are defined as $\Delta\phi=2\pi(l/q)$), therefore giving a total phase shift of $2l\pi$ over the full circle. A dynamic simulation result of the interference patterns at various distances in z-axis between a radiated vortex beam with $l=-1$ and a RHCP Gaussian beam are shown in movie S4.

Emission efficiency measurement

The experimental setup for measuring the emission efficiency of the device is shown in Fig.S3. The output of a tunable laser was coupled into Port 1 of the access waveguide using a tapered fibre lens tip, with suitable power levels controlled by a VOA. The quasi-TE mode in the waveguide was excited by controlling the input light polarisation. The optical power emitted from the input fibre lens tip is P_1. The emitted beam power Pout is collected by an objective lens and measured by the detector A. The power from Port 2 is collected by another tapered fibre lens tip. The collected power P_2 is measured by the detector B. It should be noted that the accurate value of Pout is obtained by taking into account of the insertion loss of objective lens. Suppose at Port 1 and Port 2 the same coupling loss between the fibre lens tip and the waveguide exists, the power in the mid-point of the access waveguide (where it is coupled to the micro-ring) is given by

$$P_{in} \quad (dBm) = \frac{(P_1 + P_2)}{2} \quad (dBm)$$

The emission efficiency η of the device is defined as the ratio of the emitted power over the optical power in the access waveguide, and is given as:

$$\eta = P_{out} \quad (dBm) - P_{in} \quad (dBm)$$

The above measurement has been done across the experimental wavelength range so that η is calibrated over the entire spectrum. As shown in Fig.S2 and Fig.3, η is up to 10% for the $q=36$ device and up to 13% for the $q=72$ device (the emission power are calibrated to the value when the P_{in} is 0 dBm). The fibre to waveguide transmission loss (including fibre to chip coupling and on-chip waveguide losses) is measured to be 3 dB. Therefore the fibre to emission efficiency is about 5%.

It should be noted that the 5~13% emission efficiency is the emission efficiency into each OAM state. The emission spectrum shown in Fig.3 is obtained by scanning the tunable laser to different wavelengths, and at each wavelength the emitted power and the input power are recorded. The measured data are normalised to the input power, thus the

3

emission efficiency of each OAM state can be read from the spectrum directly (as if the input optical power is 0dBm, or 1 mW). For example, in Fig.3, for l=-3, the emitted power is around -9 dBm, then the efficiency at l=-3 is calculated as η=-9dBm-0dBm=-9dB or 12.6%.

Supplementary Text

Angular momentum carried by WGMs

WGMs in circular resonators are angular momentum eigenstates and have discrete azimuthal propagation constants v_{WGM}=$\beta_p R$=p resulting from the self-consistent phase requirement for resonance under the periodic boundary condition. The integer p denotes the azimuthal mode number and physically is the number of optical periods around the resonator. R is the effective radius of the WGM, and β_p is light's propagation constants at R. The azimuthal propagation constant, frequently used in rotationally symmetric resonant devices (29), describes the optical phase shift per unit azimuthal angle. It is also a measure of angular momentum as the amount of angular momentum carried by every WGM photon is $v_{WGM}\hbar$ =$p\hbar$. Additionally, the spin angular momentum of WGM is zero, because WGM is purely linear polarized. Therefore the angular momentum carried by WGM is purely orbital.

Derivation of the Equation v_{rad}=p-q

We are interested in the coupling between the guided whispering gallery modes (WGM) and radiation modes. The coupling can be described by a coupled mode theory (CMT) in which the periodic variation of the dielectric constant is considered as a perturbation that couples the unperturbed eigen-modes of the original structure into other modes. We adapt the CMT for the cylindrical coordinate system. In an angular grating structure, the dielectric constant as a function of space is written as:

$$\varepsilon(r,z,\theta) = \varepsilon_a(r,z) + \Delta\varepsilon(r,z,\theta) \tag{s1}$$

where $\varepsilon_a(r, z)$ is the unperturbed part of the dielectric constant. $\Delta\varepsilon(r,z,\theta)$ represents the dielectric perturbation and is periodic in the θ direction and is the only periodically varying part of the dielectric constant (See Fig S4).

Since the unperturbed dielectric medium is homogeneous in the angular direction θ, in the cylindrical coordinate system (r, z, θ), the eigen-modes propagating in the θ direction in the unperturbed structure can be written in form:

$$E(r,z,\theta,t) = E_m(r,z)\exp[i(\omega t - \beta_m R\theta)] = E_m(r,z)\exp[i(\omega t - v_m\theta)] \tag{s2}$$

where E_m is the transverse mode profile of the mth eigen-mode, β_m is its propagation constant, and ω is the angular frequency corresponding to vacuum wavelength λ. The azimuthal angular behaviour of field (Equation s2) is determined by the angular

4

propagation constant $v_m=\beta_m R$. We ignore the radiation loss in a bend waveguide because it is small in SOI structures with strong optical confinement.

These eigen-modes satisfy

$$(\frac{\partial^2}{\partial r^2}+\frac{1}{r}\frac{\partial}{\partial r}+\frac{\partial^2}{\partial z^2}+\omega^2\mu\varepsilon_a(r,z)-\frac{v_m^2}{r^2})E_m(r,z)=0 \qquad (s3)$$

We now express the field in the perturbed waveguide as a linear combination of the eigen-modes of the unperturbed waveguide:

$$E=\sum_m A_m(\theta)E_m(r,z)\exp[i(\omega t-v_m\theta)] \qquad (s4)$$

where the coefficients A_m depend on θ and the summation is over all of the eigen-modes of the unperturbed bend waveguide, including not only guided modes but also radiation modes, because the guided modes together with radiation modes form a complete basis set.

We now substitute Equation s4 into the wave equation

$$[\frac{\partial^2}{\partial r^2}+\frac{1}{r}\frac{\partial}{\partial r}+\frac{\partial^2}{\partial z^2}+\frac{1}{r^2}\frac{\partial^2}{\partial\theta^2}+\omega^2\mu(\varepsilon_a(r,z)+\Delta\varepsilon(r,z,\theta))]E=0 \qquad (s5)$$

Using Equation s3 and slowly varying amplitude (SVA) approximation, we obtain

$$\sum_m -2iv_m\frac{dA_m}{d\theta}E_m(r,z)\exp(-iv_m\theta)=-\omega^2\mu r^2\sum_n \Delta\varepsilon(r,z,\theta)A_n E_n(r,z)\exp(-iv_n\theta) \qquad (s6)$$

We next take the scalar product of Equation s6 with $E_s^*(r,z)$ (complex conjugate of sth mode field) and integrate over r-z plane. The result, using the orthogonality between the eigen-modes, is

$$\langle s|s\rangle\frac{dA_s}{d\theta}=\frac{\omega^2\mu}{2iv_s}\sum_n\langle s|\Delta\varepsilon(r,z,\theta)r^2|n\rangle A_n\exp[i(v_s-v_n)\theta] \qquad (s7)$$

where

$$\langle s|s\rangle=\int E_s^*(r,z)E_s(r,z)drdz \qquad (s8)$$

$$\langle s|\Delta\varepsilon(r,z,\theta)r^2|n\rangle=\int E_s^*(r,z)\Delta\varepsilon(r,z,\theta)r^2 E_n(r,z)drdz \qquad (s9)$$

Since the perturbation $\Delta\varepsilon(r,z,\theta)$ is periodic in θ direction, we can expand it as a Fourier series:

$$\Delta\varepsilon(r,z,\theta)=\sum_{g\neq0}\varepsilon_g(r,z)\exp(igq\theta) \qquad (s10)$$

where $q = \dfrac{2\pi R}{\Lambda}$ is the number of grating elements and g is an integer. Substitution of Equation s10 into Equation s7 leads to

$$\frac{dA_s}{d\theta} = \frac{\omega^2 \mu}{2i\nu_s \langle s|s\rangle} \sum_m \sum_n \langle s|\Delta\varepsilon(r,z,\theta)r^2|n\rangle A_n \exp[i(\nu_s - \nu_n + gq)\theta] \qquad (s11)$$

Integrating Equation s11 over an arc which is much larger than the grating period Λ, yet is much smaller than the variation scale of the amplitude, we obtain the increment of the sth field amplitude, ΔA_s, due to the mode coupling with the nth mode via the gth Fourier component of the dielectric perturbation:

$$\Delta A_s = \frac{\omega^2 \mu}{2i\nu_s \langle s|s\rangle} \langle s|\Delta\varepsilon(r,z,\theta)r^2|n\rangle A_n \int\limits_{\theta R \gg \Lambda} \exp[i(\nu_s - \nu_n + gq)\theta]d\theta \qquad (s12)$$

The integral is non-vanishing only when the exponent is zero, in other words, the mode coupling between the sth mode and the nth mode is significant only when the following condition is satisfied:

$$\nu_s - \nu_n + gq = 0 \qquad (s13)$$

If mode s is a radiation mode and mode n is a guided WGM, Equation s13 can be written as:

$$\nu_{rad} = \nu_{WGM} - gq \qquad g = \pm 1, \pm 2, ... \qquad (s14)$$

Equation s14 is the angular phase matching condition and g is actually the diffraction order. In principle, a large number of modes can be involved as long as their angular wave vectors are matched for some integer g. However, in our case, the possible value for g is limited by the used material system.

Fig. S5 shows the graphical representation for the angular phase matching condition (Equation s14). Because the radiation mode is in free space, the wave vector $\beta_{rad} = \dfrac{2\pi}{\lambda}$, λ is the free space wavelength. The angular component $\beta_{rad,\theta}$ needs to satisfy the following relation:

$$\left|\beta_{rad,\theta}\right| = \left|\frac{\nu_{rad}}{R}\right| < \frac{2\pi}{\lambda} \qquad (s15)$$

On the other hand

$$\beta_{WGM} = \frac{\nu_{WGM}}{R} = \frac{2\pi}{\lambda} n_{eff} \qquad (s16)$$

6

where n_{eff} is the effective index of the WGM in the waveguide.

Substituting Equation s14 and Equation s16 into Equation s15 leads to

$$(n_{eff} - 1)\frac{\Lambda}{\lambda} < g < (n_{eff} + 1)\frac{\Lambda}{\lambda} \qquad (s17)$$

In our devices, λ is around 1550nm, Λ is around 650nm and the n_{eff} is around 2.5. g is in the order of 0.6 to 1.5, according to Equation s17. Therefore the only possible value for g is 1. Taking into account the relation of $v_{WGM}=p$, the angular phase matching condition Equation s14 can be rewritten as:

$$v_{rad} = p - q \qquad (s18)$$

States of Polarization of emitter optical field

There are at least two known SOPs associated with WGMs, a quasi-transverse electric (TE) mode with the light's predominant transverse electric-field component $\boldsymbol{E}_T$ parallel to the plane of the WGM and a quasi-transverse magnetic (TM) mode with $\boldsymbol{E}_T$ vertical to the plane of the WGM. As both WGM SOPs are cylindrically symmetric, the radiated beams must also have cylindrically symmetric SOPs. More precisely, at any point in space, the SOP of the radiated beam is determined by the SOP of the local optical field being scattered at each grating element – these will superimpose in space to give the radiation pattern. In high contrast silicon waveguides, strong electric fields in the propagation (azimuthal) direction, $\boldsymbol{E}_{az}$, are found to be present due to tight confinement (*30*). Its maxima are located at the waveguide boundaries perpendicular to the dominant transverse electric-field component $\boldsymbol{E}_T$, where $\boldsymbol{E}_T$ itself is weak and associated with large discontinuities. It can be seen that by placing the grating element at chosen locations it is possible to engineer the emitted beam SOP.

Fig. S6 shows the simulated field distribution of $\boldsymbol{E}_{az}$ and $\mathbf{E}_T$ of the quasi-TE mode in a bend waveguide with the same structure parameters of the fabricated device shown in Fig 1. The fields are calculated by a full vector three-dimensional bend waveguide mode solver (*31*). As can be seen in Fig. S6, the electric fields are predominantly in azimuthal direction at the inner wall, where the grating elements are located. Therefore the radiated beams are azimuthally polarized CV beams.

The SOPs of the radiated beams are further confirmed by a three dimensional finite difference time domain (3D-FDTD) simulation results as shown in Fig. S7. The model includes the access waveguide and the micro-ring cavity with angular grating element, exactly according to device structures used in the experiment. Fig. S7A shows the total intensity distribution ($|E_x|^2 + |E_y|^2$) of the beams with l=-2, while Fig. S7B and Fig. S7C show the distributions of $|E_x|^2$ and $|E_y|^2$, respectively. *x* axis is the horizontal direction and *y* is the vertical direction.
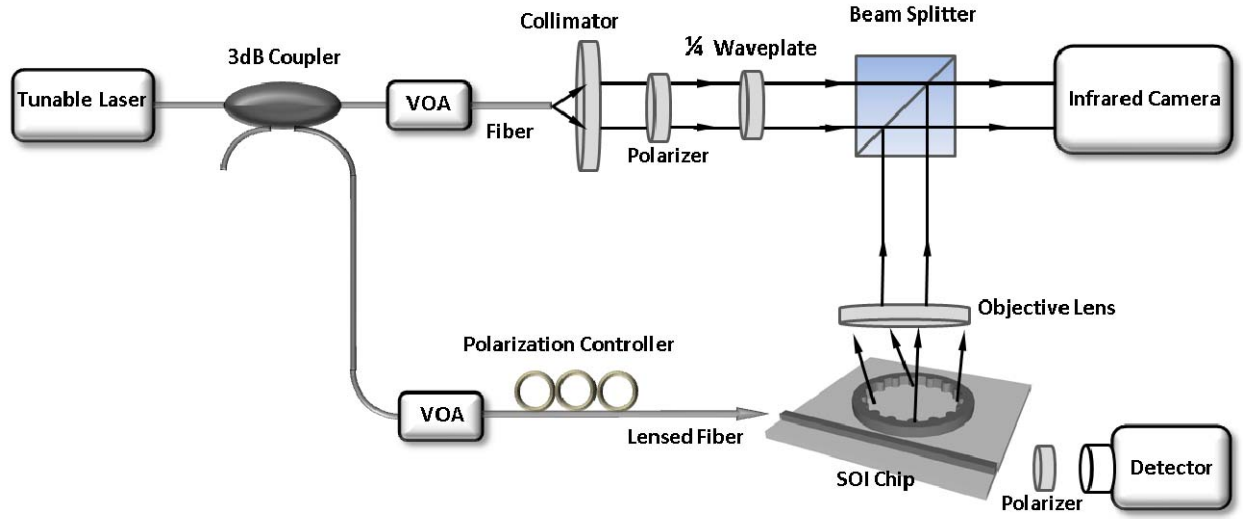
Fig. S1. The experimental setup for investigating the phase structure of the radiated beam from the SOI chip. The output of a tunable laser is split into two branches by a 3dB coupler. One branch is passed to a collimator to produce an expanded Gaussian reference beam. After going through a linear polarizer followed by a quarter-wave plate set at 45 or -45 degrees to the axis of polarization, the Gaussian beam is then LHCP or RHCP. The other branch is coupled into the input waveguide of the micro-ring resonator to excite the radiated beam carrying OAM. A polarization controller is used to launch light in the quasi-TE mode and the polarization is monitored by a polarizer followed by an optical detector placed at the output port of the waveguide. The radiated beam is collimated and then directed to a beam splitter where it is combined with the reference beam and projected onto an infrared camera.
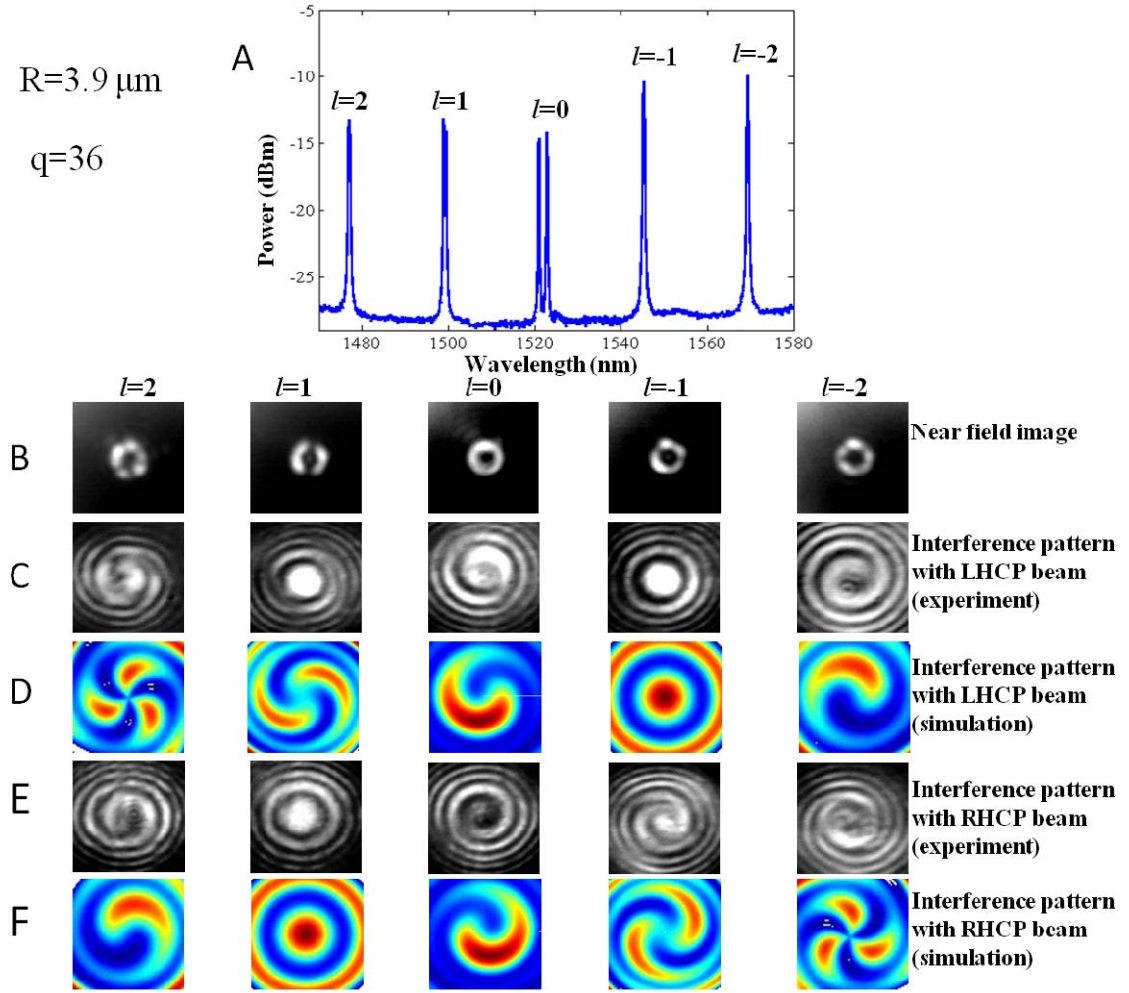
Fig. S2 (A) Measured radiation spectrum for a device with a radius of 3.9 μm. (B) Near field intensity distributions of the radiated beams. (C)-(F). Measured and simulated interference patterns with LHCP and RHCP reference beams. Row C and D have *l*-1 spirals and row E and F have *l*+1 spirals. The simulation is carried out using a dipole-emission based semi-analytical model. By placing *q* number of dipoles around the resonator circumference with their polarization moment aligned with the azimuthal direction, field patterns at any point in space can be calculated. Different *l* values are achieved by setting the phase delay between adjacent dipoles to $2l\pi/q$.
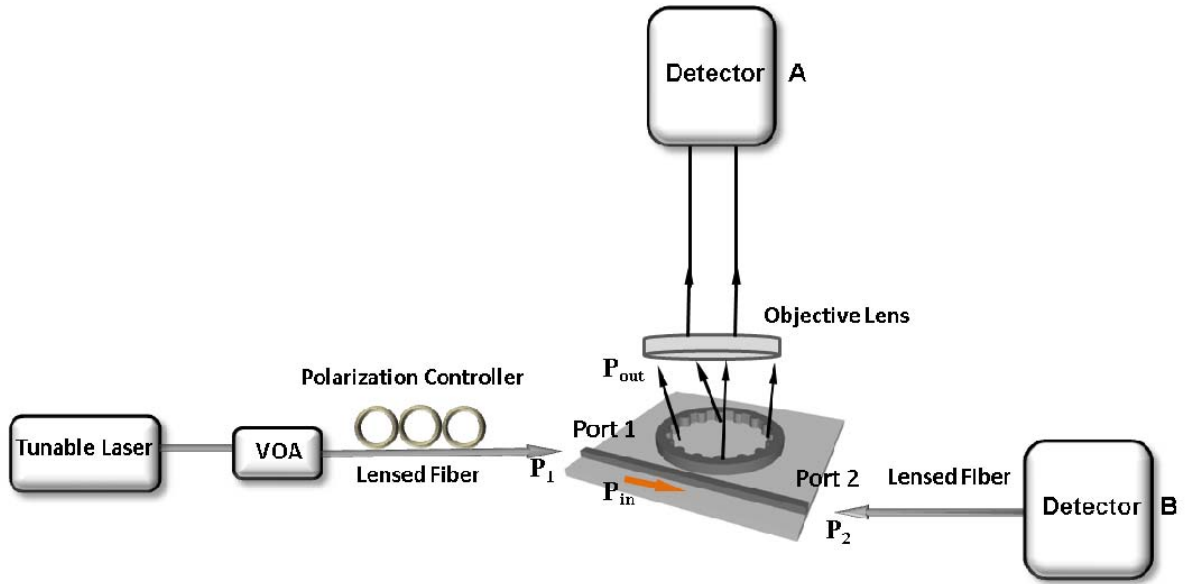
Fig. S3 The experimental setup for measuring the emission efficiency of the device. The transmission through the objective lens is separately calibrated.
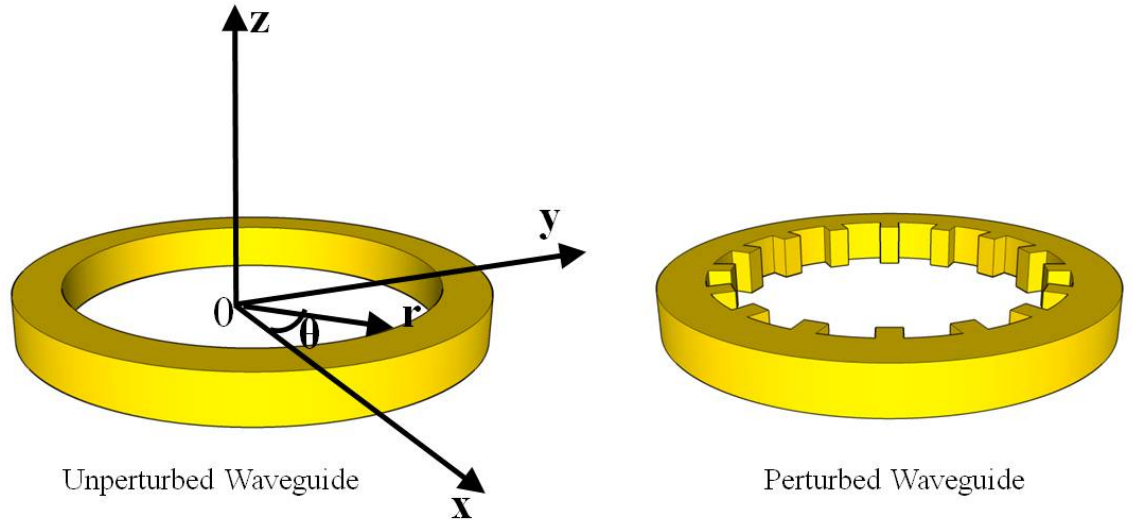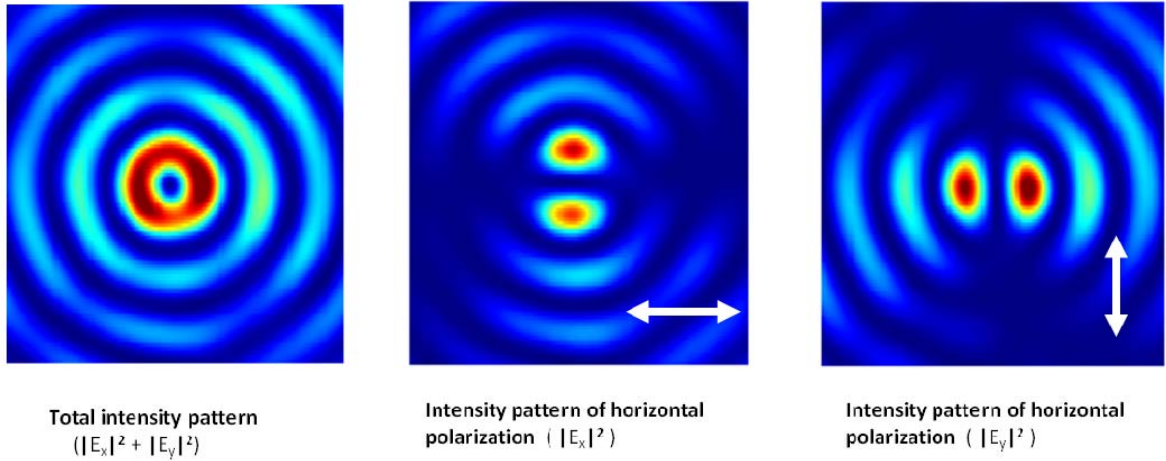
Fig. S4 (a) Unperturbed ring waveguide. (b) Perturbed ring waveguide with angular grating along the inner circumference.
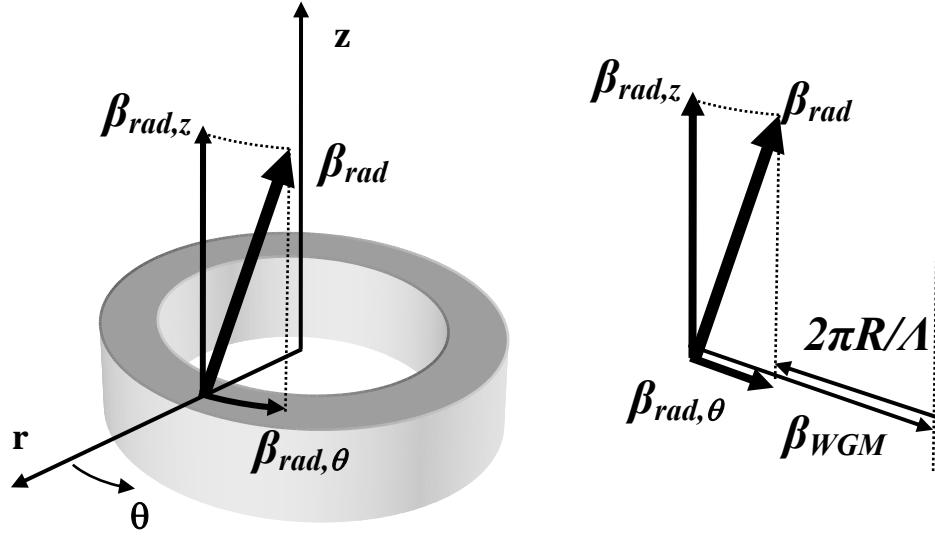
Fig. S5 Graphical representation of the angular phase matching condition at the emitter-air interface. The propagation constant of the WGM in the azimuthal direction, β_{WGM}, is partially cancelled by the grating vector $2\pi R/\Lambda$ in the diffraction process, leaving only a fraction, $\beta_{rad,\theta}$, in the azimuthal direction and giving rise to a large z-component $\beta_{rad,z}$.
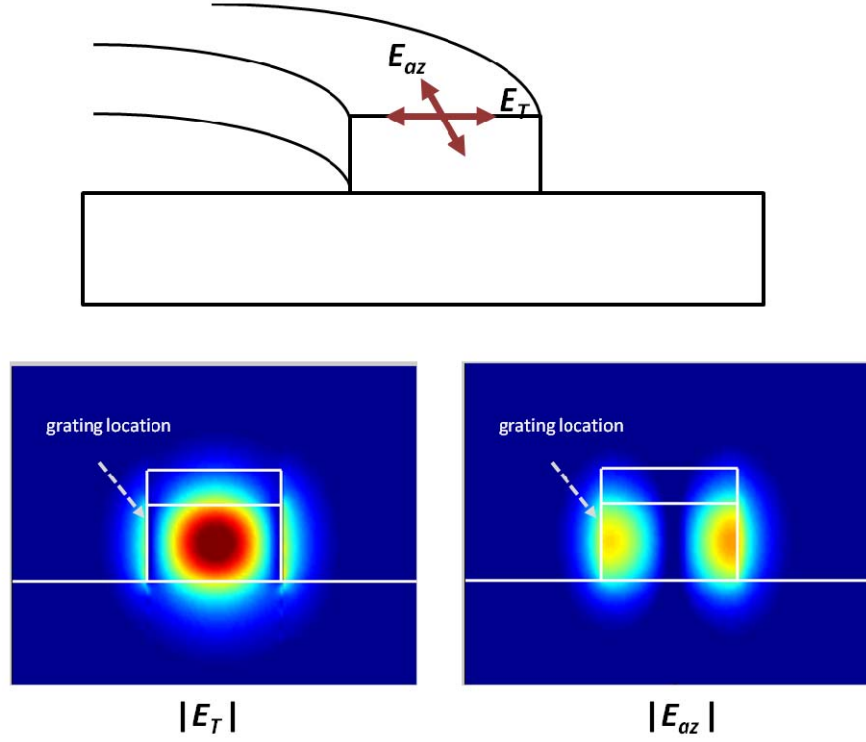
Fig. S6 Simulated field distribution of azimuthal electric field E_{az} and transverse electric field E_T for quasi-TE WGM mode in silicon bend waveguide at 1550nm. The top part shows the cross section of the bend waveguide and the lower part shows the field distribution. The grating elements are located at the inner side wall where the electric field are predominantly in azimuthal direction. A grating placed on top of the waveguide would produce predominantly radially polarised emission by mainly scattering E_T. It is therefore possible to engineer the emitted beam SOP.

Total intensity pattern
$(|E_x|^2 + |E_y|^2)$

Intensity pattern of horizontal
polarization $(|E_x|^2)$

Intensity pattern of horizontal
polarization $(|E_y|^2)$

Fig. S7. The 3D-FDTD simulation results of the intensity patterns for the radiated beam with l=-2. The total intensity (left) is a group of concentric rings. When decomposed into two orthogonal linearly polarized beams, it can be revealed that the SOP at any point is azimuthal.

Movie S1

The movie shows rotating spiral interference pattern created by disturbing the phase of a reference beam relative to that of a vortex beam with l=-4. The reference beam is a LHCP Gaussian beam. Three arms can be seen clearly in the pattern.

Movie S2

The movie shows rotating spiral interference pattern created by disturbing the phase of a reference beam relative to that of a vortex beam with l=-4. The reference beam is a RHCP Gaussian beam. Five arms can be seen clearly in the pattern.

Movie S3

The movie shows rotating spiral interference patterns created by disturbing the phase of a reference beam relative to the beams generated from the vortex emitter array. The reference beam is a RHCP Gaussian beam. The three spiral patterns are rotating synchronously.

Movie S4

The movie shows dipole based semi-analytical simulated result of the interference patterns at various distances in z-axis between a radiated vortex beam with l=-1 and a RHCP Gaussian beam.

References and Notes

1. L. Allen, M. W. Beijersbergen, R. J. C. Spreeuw, J. P. Woerdman, Orbital angular momentum of light and the transformation of Laguerre-Gaussian laser modes. *Phys. Rev. A* **45**, 8185 (1992). doi:10.1103/PhysRevA.45.8185 Medline

2. S. Fürhapter, A. Jesacher, S. Bernet, M. Ritsch-Marte, Spiral interferometry. *Opt. Lett.* **30**, 1953 (2005). doi:10.1364/OL.30.001953 Medline

3. D. G. Grier, A revolution in optical manipulation. *Nature* **424**, 810 (2003). doi:10.1038/nature01935 Medline

4. G. Gibson *et al.*, Free-space information transfer using light beams carrying orbital angular momentum. *Opt. Express* **12**, 5448 (2004). doi:10.1364/OPEX.12.005448 Medline

5. N. K. Fontaine, C. R. Doerr, L. Buhl, in *Optical Fiber Communication Conference*, *OSA Technical Digest* (Optical Society of America, Washington DC, 2012), paper OTu1l.2.

6. A. Mair, A. Vaziri, G. Weihs, A. Zeilinger, Entanglement of the orbital angular momentum states of photons. *Nature* **412**, 313 (2001). doi:10.1038/35085529 Medline

7. G. Molina-Terriza, J. P. Torres, L. Torner, Twisted photons. *Nat. Phys.* **3**, 305 (2007). doi:10.1038/nphys607

8. N. R. Heckenberg, R. McDuff, C. P. Smith, A. G. White, Generation of optical phase singularities by computer-generated holograms. *Opt. Lett.* **17**, 221 (1992). doi:10.1364/OL.17.000221 Medline

9. M. W. Beijersbergen, R. P. C. Coerwinkel, M. Kristensen, J. P. Woerdman, Helical-wavefront laser beams produced with a spiral phaseplate. *Opt. Commun.* **112**, 321 (1994). doi:10.1016/0030-4018(94)90638-6

10. L. Marrucci, C. Manzo, D. Paparo, Optical spin-to-orbital angular momentum conversion in inhomogeneous anisotropic media. *Phys. Rev. Lett.* **96**, 163905 (2006). doi:10.1103/PhysRevLett.96.163905 Medline

11. G. Biener, A. Niv, V. Kleiner, E. Hasman, Formation of helical beams by use of Pancharatnam-Berry phase optical elements. *Opt. Lett.* **27**, 1875 (2002). doi:10.1364/OL.27.001875 Medline

12. N. Yu *et al.*, Light propagation with phase discontinuities: Generalized laws of reflection and refraction. *Science* **334**, 333 (2011). doi:10.1126/science.1210713 Medline

13. M. Smit, J. van der Tol, M. Hill, Moore's law in photonics. *Laser Photon. Rev.* **6**, 1 (2012). doi:10.1002/lpor.201100001

14. C. R. Doerr, L. L. Buhl, Circular grating coupler for creating focused azimuthally and radially polarized beams. *Opt. Lett.* **36**, 1209 (2011). doi:10.1364/OL.36.001209 Medline

15. K. J. Vahala, Optical microcavities. *Nature* **424**, 839 (2003). doi:10.1038/nature01939 Medline

16. Materials and methods are available as supplementary materials on *Science* Online.

17. A. B. Matsko, A. A. Savchenkov, D. Strekalov, L. Maleki, Whispering gallery resonators for studying orbital angular momentum of a photon. *Phys. Rev. Lett.* **95**, 143904 (2005). doi:10.1103/PhysRevLett.95.143904 Medline

18. D. Taillaert *et al*., Grating couplers for coupling between optical fibers and nanophotonic waveguides. *Jpn. J. Appl. Phys.* **45**, 6071 (2006). doi:10.1143/JJAP.45.6071

19. R. Dorn, S. Quabis, G. Leuchs, Sharper focus for a radially polarized light beam. *Phys. Rev. Lett.* **91**, 233901 (2003). doi:10.1103/PhysRevLett.91.233901 Medline

20. Z. Bomzon, V. Kleiner, E. Hasman, Pancharatnam—Berry phase in space-variant polarization-state manipulations with subwavelength gratings. *Opt. Lett.* **26**, 1424 (2001). doi:10.1364/OL.26.001424 Medline

21. A. Niv, G. Biener, V. Kleiner, E. Hasman, Manipulation of the Pancharatnam phase in vectorial vortices. *Opt. Express* **14**, 4208 (2006). doi:10.1364/OE.14.004208 Medline

22. I. Moreno, J. A. Davis, I. Ruiz, D. M. Cottrell, Decomposition of radially and azimuthally polarized beams using a circular-polarization and vortex-sensing diffraction grating. *Opt. Express* **18**, 7173 (2010). doi:10.1364/OE.18.007173 Medline

23. A. Yariv, Universal relations for coupling of optical power between microresonators and dielectric waveguides. *Electron. Lett.* **36**, 321 (2000). doi:10.1049/el:20000340

24. Y. Yu, R. O'Dowd, *IEEE Photon. Technol. Lett.* **14**, 1397 (1992).

25. S. Manipatruni, Q. Xu, M. Lipson, PINIP based high-speed high-extinction ratio micron-size silicon electrooptic modulator. *Opt. Express* **15**, 13035 (2007). doi:10.1364/OE.15.013035 Medline

26. K. Ladavac, D. Grier, Microoptomechanical pumps assembled and driven by holographic optical vortex arrays. *Opt. Express* **12**, 1144 (2004). doi:10.1364/OPEX.12.001144 Medline

27. D. S. Weiss *et al*., Splitting of high-Q Mie modes induced by light backscattering in silica microspheres. *Opt. Lett.* **20**, 1835 (1995). doi:10.1364/OL.20.001835 Medline

28. T. J. Kippenberg, S. M. Spillane, K. J. Vahala, Modal coupling in traveling-wave resonators. *Opt. Lett.* **27**, 1669 (2002). doi:10.1364/OL.27.001669 Medline

29. L. Prkna, M. Hubalek, J. Ctyroky, Field modeling of circular microresonators by film mode matching. *IEEE J. Sel. Top. Quantum Electron.* **11**, 217 (2005). doi:10.1109/JSTQE.2004.841716

30. J. B. Driscoll *et al*., Large longitudinal electric fields (E_z) in silicon nanowire waveguides. *Opt. Express* **17**, 2797 (2009). doi:10.1364/OE.17.002797 Medline

31. X. Cai, D. Huang, X. Zhang, Numerical analysis of polarization splitter based on vertically coupled microring resonator. *Opt. Express* **14**, 11304 (2006). doi:10.1364/OE.14.011304 Medline